

Full length article

Irradiation induced creep in nanocrystalline high entropy alloys

Gowtham Sriram Jawaharram^a, Christopher M. Barr^b, Anthony M. Monterrosa^b,
Khalid Hattar^b, Robert S. Averback^a, Shen J. Dillon^{a,*}

^a Department of Materials Science and Engineering, University of Illinois Urbana-Champaign, Urbana, IL, United States

^b Sandia National Laboratories, PO Box 5800-1056, Albuquerque, NM 87185, United States



ARTICLE INFO

Article history:

Received 22 July 2019

Revised 4 October 2019

Accepted 15 October 2019

Available online 19 October 2019

Keywords:

High entropy alloy (HEA)

Irradiation induced creep

Vacancy migration enthalpy

In situ transmission electron microscopy

ABSTRACT

Irradiation induced creep (IIC) compliance in NiCoFeCrMn high entropy alloys is measured as a function of grain size ($30 < x < 80$ nm) and temperature (23–500 °C). For 2.6 MeV Ag³⁺ irradiation at a dose rate of 1.5×10^{-3} dpa⁻¹s⁻¹ the transition from the recombination to sink limited regimes occurs at ~ 100 °C. In the sink-limited regime, the IIC compliance scales inversely with grain size, consistent with a recently proposed model for grain boundary IIC. The thermal creep rate is also measured; it does not become comparable to the IIC rate, however, until ~ 650 °C. The results are discussed in context of defect kinetics in irradiated HEA systems.

© 2019 Acta Materialia Inc. Published by Elsevier Ltd. All rights reserved.

1. Introduction

The lack of materials suitable for the extreme environments associated with next-generation nuclear reactors imposes major constraints on the viability of this source of carbon-free energy [1–3]. A variety of strategies have been employed to develop structural materials appropriate for high temperature, high stress, and high displacement damage environments, but nearly all try in some manner to facilitate efficient recombination of irradiation induced vacancies and interstitials [4,5]. Most recent attempts to achieve this focus on the introduction of a high density of incoherent interfaces; such as in oxide dispersion strengthened alloys [6–9], multilayer nanolaminates [10–15], and self-organized precipitation in nanocrystalline alloys [16–19]. Solid-solutions can also promote recombination via point defect trapping, although strong solute-defect interactions tend to also promote radiation induced segregation [20–24]; see refs. [25,26] for a detailed discussion. Certain high entropy alloys (HEAs) and other concentrated solid solutions have recently been reported to be less susceptible to radiation damage than more conventional alloys, [27–29]. For example, HEAs have been reported to offer improved swelling resistance [30,31] and smaller dislocation loop structures [30,32]. In a comparative study by Jin et al., swelling in NiCoFeCrMn was only ~0.2% but ~6.7% in Ni under the same conditions [31]. It was hypothesized that the enhanced lattice strain in HEAs promoted slug-

gish diffusion of defects [33,34], hindered dislocation movement [35] and suppressed the one-dimensional motion of interstitial clusters along the FCC <110> direction, thus promoting interstitial – vacancy recombination [30]. Aside from enhanced tolerance to irradiation, HEAs exhibit high strength and ductility, additional requirements for structural materials in next-generation reactors [36,37]. Presently, however, irradiation induced creep (IIC) response and radiation enhanced diffusion in five component HEAs, have yet to be measured. Oxide dispersion strengthened steels [38,39], nanolaminates [10], and nanocrystalline alloys [40,41], for example, have all been shown to be susceptible to IIC to varying degrees depending on their microstructure and materials properties.

Measurements of IIC are typically quite limited in new materials owing to the associated experimental challenges. Such measurements generally require bulk specimens and consequently employ neutron irradiations. In-reactor experiments, however, generally require extended measurement times to achieve high damage levels and special handling of radioactive samples, both adding greatly to the cost of the research. Electron and ion irradiations provide an attractive alternative to neutrons, but both create other challenges. For charged particle irradiations, there is a tradeoff between high penetration range, which is conducive to testing of large samples, and high nuclear stopping power, which provide a high damage level [42,43]. As a result, testing large samples to damage levels greater than a few displacements per atom (dpa) is difficult using light ions and electrons. Light ions and electrons, moreover, do not simulate damage from fast neutrons, owing to their unscreened coulombic interactions with target atoms [10,40,41,44–46]. Heavy ions simulate neutron damage far more

* Corresponding author.

E-mail address: sdillon@illinois.edu (S.J. Dillon).

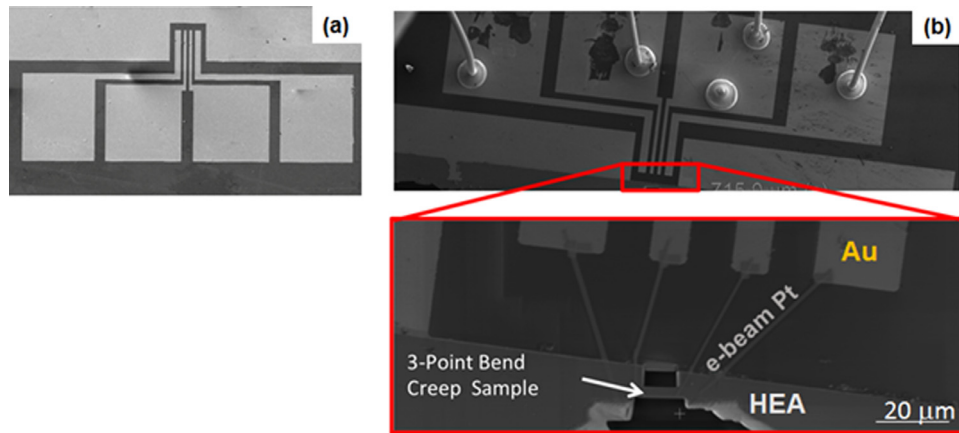


Fig. 1. (a) Au lines and pads fabricated on an oxidized Si wafer using the thin film lift-off process and (b) Au wire bonds are used to connect the Au pads to the Vespel[®] mechanical test stage and the focused ion beam was used to fabricate the HEA 3-point bend creep sample which was connected to the Au lines using e-beam assisted Pt deposition.

closely, but they typically restrict sample sizes to less than some hundreds of nanometers. Recent experiments [10,46] have shown, however, heavy ions can be used for IIC measurements using micropillar compression specimens in conjunction with laser heating, and *in situ* transmission electron microscopy (TEM). This allowed for the measurement of IIC compliance, $B = \frac{1}{\sigma_0} \frac{d\epsilon}{d\phi}$, where $\frac{d\epsilon}{d\phi}$ is the normalized creep rate $d\epsilon/d\phi = [(d\epsilon/dt)/d\phi/dt]$, ϕ is the ion dose measured in displacements per atom (dpa), and σ_0 is the applied stress.

The current work focuses on understanding the IIC response of nanocrystalline NiCoFeCrMn HEA alloy films, ≈ 450 nm thick, as a function of temperature and grain size. It uses a three-point bending geometry on cantilever beams fabricated from thin-film specimens. The samples in this work, notably, are connected to a 4-probe electrical resistance measurement for a direct calibration of the specimen temperature. As we will show, the IIC rate in the sink limited regime scales with inverse grain size, and the magnitude of the IIC compliance of the HEA alloy is comparable to prior measurements made on Cu-W alloys of comparable grain size. The results are interpreted in the context of a grain boundary model for creep in irradiated nanocrystalline materials [47].

2. Experimental procedure

The specimens for this study were prepared by first patterning ~ 25 μm wide Au lines with contact pads on oxidized Si wafers using thin film lift-off photolithography (see Fig. 1(a)). Approximately 1 μm thick (NiCoFeCrMn) films were then grown adjacent to the Au lines using DC magnetron sputtering from a high purity ($> 99.95\%$) NiCoFeCrMn target (AJA, USA) at a base pressure of $\sim 5 \times 10^{-8}$ torr and an Ar pressure of $\sim 3 \times 10^{-3}$ torr. The samples were subsequently polished from the back (Si) side of the substrate to reduce the substrate thickness to ≈ 20 – 25 μm . At this point, the samples were transferred to a custom Vespel[®] mechanical test specimen stage and the Au pads on the sample were wire bonded to the Au pads grown on the specimen stage.

A Helios 600i Nanolab or a Scios2 dual-beam FIB operating at 30 kV was next used to shape the microbeams for the bending tests. Typically, a dozen microbeams were fabricated on each Si wafer. The milling currents were initially 2.5 nA but reduced to 40 pA for final polishing. Finally, a single bending beam, used for temperature calibration, was connected to the Au lines on the sample using electron beam induced deposition of Pt. The platinum thickness was approximately 1 μm . The final dimensions of the beams were maintained approximately constant: length = 10 ± 1.5 μm , width = 1.0 ± 0.2 μm and

thickness = 450 ± 100 nm. The temperature dependence of electrical resistance was calibrated in a tube furnace under vacuum. It should be noted that the beams calibrated *ex situ* were separate from the samples calibrated *in situ*, but the *ex situ* calibration results were found reproducible across multiple beams of similar dimensions, as expected.

In situ TEM based creep testing was performed in the I³TEM, which is a customized 200 keV JEOL 2100 LaB₆ TEM at Sandia National Laboratories [48]. The TEM is connected to a 6 MeV Tandem accelerator, which is used for *in situ* irradiation. The ion beam impinges the sample nearly perpendicular to the electron beam. Experiments were performed with the samples tilted 20° about the specimen rod axis toward the ion beam, such that both the electron and ion beams impinge on the sample in coincidence. The HEA microbeams were irradiated using 2.6 MeV Ag³⁺ ions operating at current densities between 2.4×10^{-2} and 3.0×10^{-2} A-m⁻² producing dose rates between 1.5×10^{-3} and 1.9×10^{-3} dpa-s⁻¹ (refer to supplementary Fig. S1 for the thickness dependence of the dose rate calculated with SRIM 2013). SRIM calculations suggest that the concentration of Ag ions implanted over several hours, during which experiments were performed, is on the order of 10^{-3} . A 1064 nm IR laser with a nominal diameter of ≈ 100 μm and a maximum power of 20 W was used as the heating source. The laser's 33 kHz pulse rate is fast relative to the thermal relaxation time, $\tau = 0.08$ s of the system, thus the temperature is anticipated to reach a steady-state (see supplementary Fig. S2). The temperature of the sample was varied by the applying laser power between 1 W and 4.8 W. The chamber pressure was maintained at $\approx 10^{-5}$ torr. Constant mechanical loading was applied with a Hysitron PI-95 picoindenter using stress-jump tests in the range 50–900 MPa with the load held constant for 300 s after each stress jump (typical strains are 10^{-3} – 10^{-2} per stress step). The strain response was measured by both the Hysitron PI-95 indenter, and direct image-based measurements of displacement. The stresses discussed herein are the contact stresses and the strain is calculated using the flexural strain formula, $\epsilon = \frac{6w\delta}{L^2}$, where δ is the deflection of the beam at the center of the diamond punch and L and w are the length and the width of the microbeam. The beam deflections measured manually from snapshots obtained from the *in situ* videos are more accurate than the instrumented measurements, since they are less sensitive to thermal drift (see supplementary Fig. S3 for a comparison of the creep strain obtained from the Hysitron PI-95 instrument and *in situ* snapshots). The creep strain is calculated by assuming the final elastic strain during unloading is linear and subtracting it from the total strain, correcting for variation in the bending angle. Prior to the creep experiments,

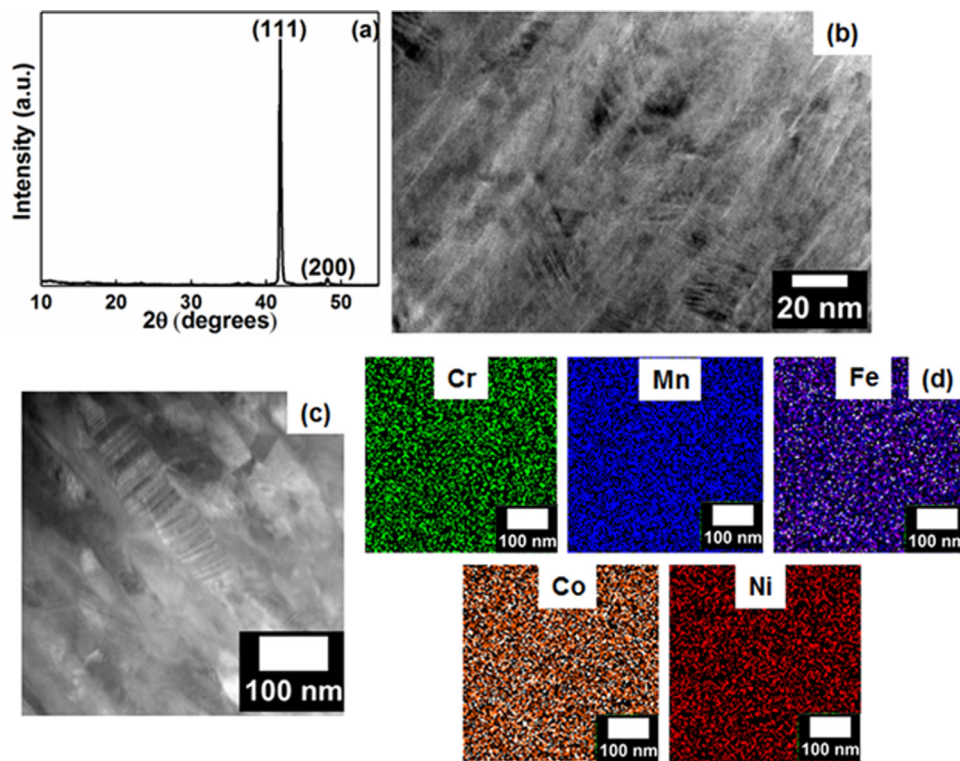


Fig. 2. (a) XRD pattern of the as-deposited HEA film in cross-section, (b) BF-TEM image of the as-deposited film showing an average grain size of 28 nm, (c) HAADF-STEM image and (d) EDS map of the as-deposited film. No significant segregation was observed in (d) indicating the homogeneous solid solution nature of the as-deposited film.

the resistance of the calibration microbeam was measured during *in situ* heating at different laser powers and compared with the *ex situ* data, thus relating specimen temperature to laser power.

Samples were tested at a 20° tilt angle to ensure the ion beam impinges on the sample (refer to supplementary Fig. S4 for a schematic view of the experimental setup). As a result, determination of the exact center of the sample has some associated uncertainty. FEM simulations showed, however, that even a large misalignment, 30%, results in an error in the stress state by only 15%. An assumption in our analysis is that the stress is approximately constant during creep. This was also tested via FEM simulations and the error was found to be on the order of 3% for displacements < 200 nm. These errors are discussed in more detail in the supplementary information.

In addition to the HEA microbeams, HEA films were also grown on (100) oriented yttria stabilized zirconia (YSZ) single crystals to measure the effect of pillar size on yield strength. HEA nanopillars with square cross-sectional areas with sides, l , between 150 and 500 nm, were fabricated using the same FIB system mentioned above, but with a final milling current of 10 pA. The aspect ratio (ratio of l to pillar length) of all pillars was maintained between 1:2 and 1:3. The nanopillar compression experiments were performed under displacement control mode at a rate of 1 nm s⁻¹. All high temperature pillar compression tests were performed at a laser power of 1.6 W. The temperature of these pillars was not determined directly, however the samples were estimated to be at similar temperatures as those grown on Si at equivalent laser powers $T \approx 55$ °C. This is supported by finite element simulations of this testing geometry, which showed SiO₂ on Si substrates was not the primary thermal impedance in these samples. As a result, the difference in substrate is expected to have little impact and any effect of the YSZ substrate would be to increase the temperature; *i.e.* $T \approx 55$ °C could be considered a lower bound estimate. At least three different pillars were tested for each experimental condition.

To determine the change in grain size during high temperature irradiation, the beams were isochronally annealed under constant irradiation flux. The hold time at each temperature (laser power) was 120 s. The mean grain size was determined from the *in situ* snapshots using the lineal intercept method as $\bar{d} = 1.39 \frac{L}{N}$, where \bar{d} is the mean grain size, L is the length of the line, N is the number of grain boundaries intersected by the line and 1.39 is a stereological correction factor. Additional *ex situ* microstructural characterization on the deformed beams was performed using a JEOL – 2010 LaB₆ TEM and a probe corrected JEOL – 2200 FS scanning transmission electron microscope (STEM).

3. Experimental results

3.1. Morphology of the as-deposited films

Fig. 2(a) shows an X-ray diffraction pattern obtained from the as-deposited HEA film. The as-deposited films were (111) textured with no secondary phases present. Bright field TEM micrographs of the as-grown films, Fig. 2(b), show columnar grains with an average in-plane grain size, $d = 28 \pm 2$ nm. The cross-sectional TEM micrographs also show a high density of twins in the as-deposited film, consistent with other studies on sputter deposited FCC alloys. During creep testing the columnar growth direction is perpendicular to the applied stress. The absence of precipitates in the HEA film was confirmed using high angle annular dark field (HAADF)-STEM imaging and EDS mapping, Fig. 2(c) and 2(d), respectively.

3.2. Temperature calibration of microbeams

Electrical resistivity measurements on the HEA microbeams during *ex situ* furnace heating and *in situ* laser heating are shown in Fig. 3(a) and (b) as a function of temperature and laser power, respectively. Comparison of these results calibrates microbeam

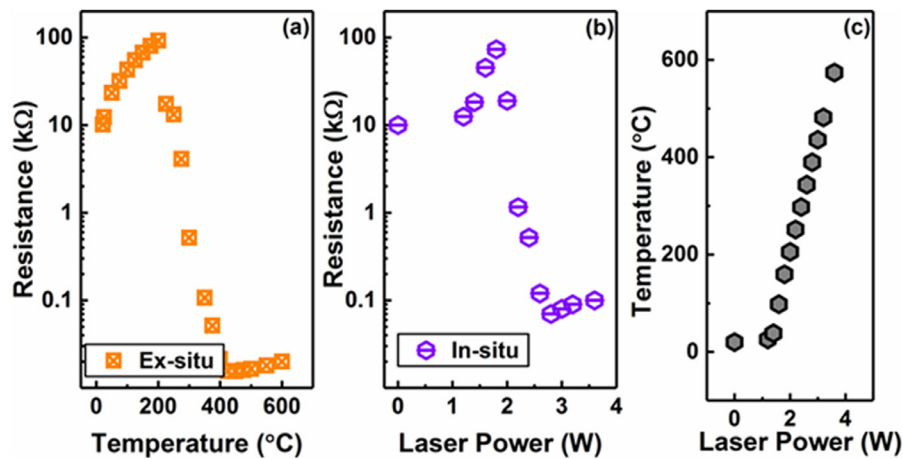


Fig. 3. Variation of resistance with (a) temperature during *ex situ* calibration and (b) laser power during *in situ* calibration of a HEA microbeam and (c) is the variation of temperature with laser power.

temperature against applied laser power, Fig. 3(c), which was measured during IIC tests. It is noteworthy that the resistance of the HEA microbeams initially increases with temperature, as expected for metals, but drops rapidly between $\approx 200^\circ\text{C}$ and 425°C and then tends to increase gradually beyond this temperature. This behavior was reversible, and hence any effect of grain growth or other thermally induced irreversible reactions on resistivity could be ruled out. The exact cause of this phenomenon was not explored; however, it was confirmed via *in situ* electron diffraction that no crystallographic phase transition occurred in this temperature range.

3.3. Pillar yield strength

26 HEA pillars were tested in compression under various experimental conditions including as-grown, pre-irradiated at room temperature, *in situ* irradiation at room temperature, *in situ* laser heating only, and combined *in situ* laser heating and irradiation; see supplementary Figs. S5 and S6. The yield strength in these pillars was determined as the deviation from the linear (elastic) region of the stress–strain curve, in order to provide a lower bound value for the yield strength. A detailed discussion of the yielding behavior is outside of the scope of this work. The main conclusions relevant to the IIC experiments are; no significant pillar size effect was observed for diameters between $\approx 100\text{ nm}$ and $\approx 450\text{ nm}$, and the lowest average yield strength for any condition tested was $\sigma_y = 1.6 \pm 0.2\text{ GPa}$. All *in situ* IIC experiments were performed at less than 26% of this value in order to be certain that plasticity occurs only via creep.

3.4. Grain size evolution under high temperature irradiation

In situ TEM imaging was performed on beams that were less than 100 nm thick to determine the grain size as a function of irradiation temperature. The results are shown in Fig. 4 along with corresponding bright-field TEM (BF-TEM images). The grain size increases from $28 \pm 2\text{ nm}$ at room temperature to $65 \pm 6\text{ nm}$ at 480°C . No defect loops or stacking fault tetrahedra are observed during the *in situ* imaging.

3.5. Irradiation induced creep testing of HEA microbeams

Examples of *in situ* IIC measurements are shown in Fig. 5. In Fig. 5(a) strain is plotted as a function of time for samples tested at different stresses and temperatures between 97°C and 480°C .

Notice that the stress is increased in steps every $\sim 300\text{ s}$. Fig. 5(b) shows that the IIC strain rate increases roughly linearly with stress, while Fig. 5(c)–(f) shows images of the microbeams before and after IIC at 97°C and 480°C . The IIC strain varies approximately linearly with time, consistent with steady-state creep. For the sample tested under room temperature (RT) irradiation (laser beam turned off), the creep strain was small, in fact, the total creep strain in the RT irradiated sample is comparable to the image pixel size, i.e. the noise level, and no further analysis for this specific irradiation condition was performed. The creep strain rate initially increases rapidly with increasing temperature from RT to $\sim 97^\circ\text{C}$, but above 97°C the creep strain rate tends to decrease slowly with increasing temperature. The initial increase in creep compliance is anticipated to occur as diffusion mediating defects become mobile. With increasing temperature these defects migrate increasingly further before recombination, resulting in more diffusion. At a critical temperature the defects can all migrate to sinks prior to recombination; this occurs at $T \sim 97^\circ\text{C}$ in our experiments. The weak temperature dependence above 97°C can be seen in Fig. 5(c) and Fig. 5(e), which show the beam deflections at 205°C and 480°C after exposure to the same loading schedule. As will be discussed below, the decrease in creep rate above 97°C results from grain growth. Post-mortem BF-TEM imaging of the strained HEA microbeams failed to show irradiation induced voids, precipitates or point defect loops; supplementary Fig. S7 shows representative images.

The grain sizes of the HEA beams during IIC in the aforementioned samples are not independently controlled but are rather a result of high temperature irradiation. To account for the effect of grain size, select beams were initially pre-annealed at 750°C for approximately 10 min to promote grain growth. IIC experiments were then performed on these pre-annealed beams at two different lower temperatures (97°C and 205°C). As seen in supplementary Fig. S8, significantly lower creep strain was observed in the pre-annealed beams as compared to the as-deposited beams tested at similar temperature in Fig. 5(a). The IIC compliances of both sample sets are discussed in more detail below.

Bending experiments were also performed on samples using laser heating in absence of irradiation to determine the thermal creep (TC) in these HEA samples. Strain versus time curves for these experiments are shown in Fig. 6(a). The stresses used to measure thermal creep, $300\text{--}900\text{ MPa}$, were significantly greater than those employed to measure IIC, $50\text{--}400\text{ MPa}$. The TC strains for stresses $< 500\text{ MPa}$ are negligible in the temperature range used to measure IIC, the two becoming comparable only at

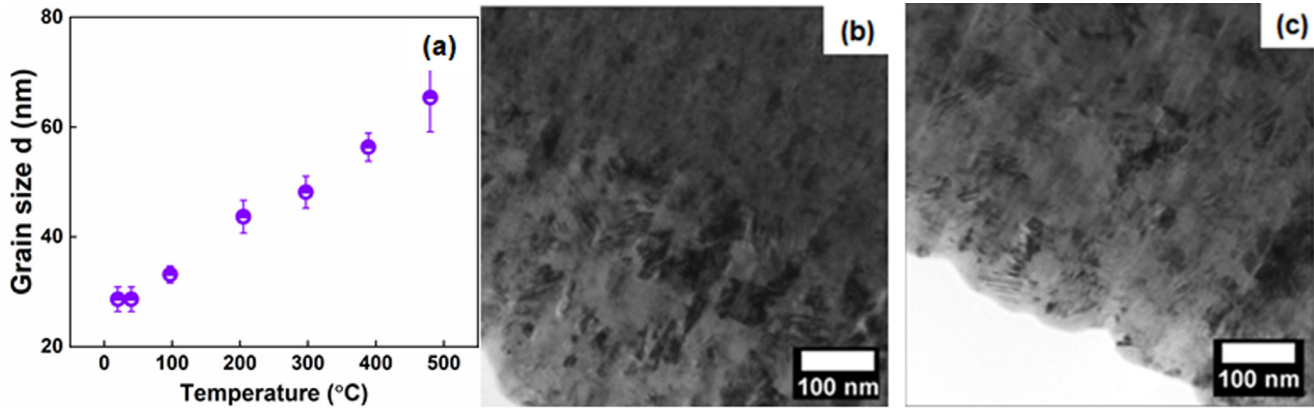


Fig. 4. (a) Change in grain size as a function of temperature, (b) and (c) are the corresponding *in situ* BF-TEM images at 97 °C and 205 °C.

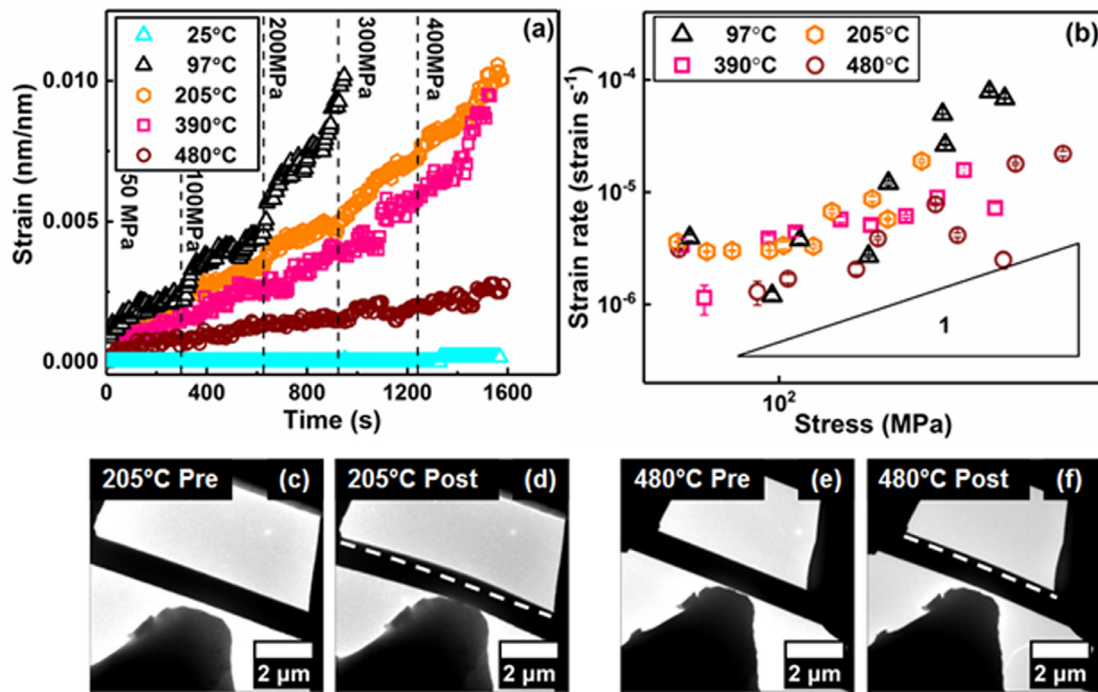


Fig. 5. (a) Variation of IIC strain with time for HEA microbeams tested at different temperatures. Loading regimes are separated by dashed lines. Negligible strain was observed in the samples tested at room temperature while beams tested at higher temperatures showed a linear temporal dependence of creep strain consistent with steady-state creep behavior. (b) shows the linear dependence of IIC strain rate with stress. (c) and (d) are the pre and post creep snapshots of a beam tested at 205 °C and (e) and (f) are the corresponding snapshots of a beam tested at 480 °C. The dotted lines in (d) and (f) represent the initial position of the beams.

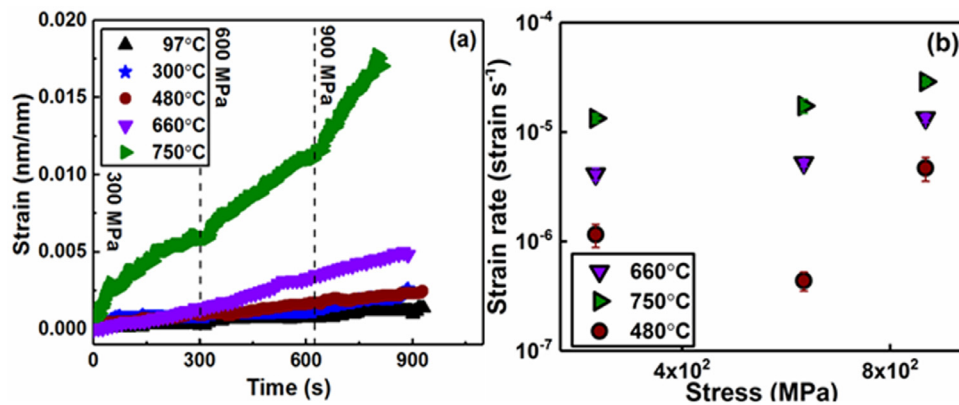


Fig. 6. (a) Variation of thermal creep strain with time for HEA microbeams tested at different temperatures. Loading regimes are separated by dashed lines. Negligible strain was observed in the samples tested below 650 °C. (b) is the variation of thermal creep strain rate with stress.

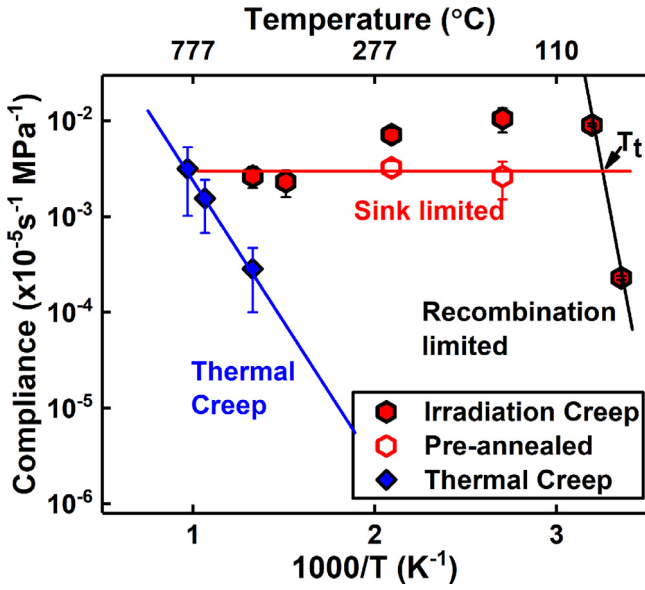


Fig. 7. Variation of creep compliance with temperature of the as-deposited, pre-annealed HEA beams tested under irradiation and thermal conditions. Below $T_t \approx 100$ °C samples are in the recombination regime. For samples of approximately equivalent grain size, $G \approx 70$ nm, the creep compliance is approximately constant in the sink limited regime, $T > T_t$. Thermal creep (TC) becomes dominant above ≈ 650 °C. (For interpretation of the references to color in this figure legend, the reader is referred to the web version of this article.)

temperatures exceeding 650 °C, see Fig. 7. TC only becomes appreciable at stresses below 900 MPa at temperatures above 660 °C (refer to Fig. 6(b)). An apparent activation energy of 0.57 ± 0.1 eV was measured for thermal creep. Thus, TC is negligible compared to IIC below 660 °C, where IIC has been measured in this work. The samples were not tested at higher temperatures, since surface oxidation was observable above 750 °C.

The variation of creep compliance with temperature, both TC and IIC, is shown on an Arrhenius plot in Fig. 7. The error bars in the compliances are the standard deviation in slope averaged across at least two different microbeams. Due to the limited number of different stresses tested in the low stress regime during TC, the compliance values for the TC measurements are obtained by dividing the strain rate by the corresponding stress. The IIC compliance of the as-deposited samples initially increases rapidly with an increasing temperature, is approximately constant between 97 °C and 200 °C, and then decreases slowly at higher temperatures. The gradual decrease in compliance above 200 °C appears to correlate with the increasing grain size. This hypothesis was tested by measuring the compliance of samples pre-annealed at temperatures $T > 480$ °C. Pre-annealing increased the grain size in the as-prepared sample to sizes very similar to those in the samples irradiated at 480 °C. As seen in Fig. 7, the creep compliances in samples having the same grain size are independent of irradiation temperature for $T_t > 100$ °C.

4. Discussion

4.1. Calculation of vacancy migration enthalpy in the HEA

We begin our discussion by recalling that IIC is negligible during irradiation at room temperature, while TC is negligible below 480 °C; we can conclude therefore that IIC is mediated by radiation-enhanced diffusion (RED) processes. Models of IIC involving RED generally begin with standard reaction rate theory to ob-

tain point defect concentrations, i.e.,

$$\frac{\partial c_{i(v)}}{\partial t} = 0 = \xi_{FM} K_0 - \frac{4\pi r_{iv}}{\Omega} (D_i + D_v) c_{i(v)} c_{v(i)} - \frac{3\pi^2}{(d)^2} D_{i(v)} c_{i(v)} - \frac{\pi^2}{(l)^2} D_{i(v)} c_{i(v)} - \frac{4\pi r_L}{\ln(8r_L/r_c)} D_{i(v)} c_{i(v)} c_L \quad (1)$$

where $c_{i(v)}$ and $D_{i(v)}$ are the concentration and diffusivities of the interstitials (vacancies), K_0 and ξ_{FM} are the defect production rate and the efficiency for producing freely migrating defects, respectively. r_{iv} , Ω , d , and l are the vacancy-interstitial recombination radius, the atomic volume, grain size, and thickness of the HEA microbeam, respectively. r_L , r_c and c_L are the dislocation loop radius, dislocation core radius and concentration of dislocation loops, respectively. The first term ($\xi_{FM} K_0$) on the right is thus the production rate of freely migrating defects. The second term ($\frac{4\pi r_{iv}}{\Omega} (D_i + D_v) c_{i(v)} c_{v(i)}$) describes the recombination rate. The third term ($\frac{3\pi^2}{(d)^2} D_{i(v)} c_{i(v)}$) describes annihilation at grain boundary sinks, assuming approximately cubic grains. The fourth term describes annihilation at the free surfaces ($\frac{\pi^2}{(l)^2} D_{i(v)} c_{i(v)}$), and the final term ($\frac{4\pi r_L}{\ln(8r_L/r_c)} D_{i(v)} c_{i(v)} c_L$) describes annihilation at dislocation

loops produced by irradiation. In large grain samples, the biased annihilation of vacancies and interstitials at dislocation loops controls IIC, e.g., stress induced preferential absorption (SIPA). Dislocation loops, however, are not thought to be stable in nanocrystalline materials, and indeed TEM observations of our samples do not reveal dislocations. We thus drop this term from Eq. (1). Since the annihilation of point defects at surfaces or by recombination cannot cause creep, we assume that it is the flux of point defects to grain boundaries that controls IIC. Furthermore, the flux of point defects to the grain boundaries *versus* the surface ($\frac{J_{GB}}{J_s}$) can be obtained by taking the ratio of the third and fourth term on the right in Eq. (1). This ratio assuming $d = 70$ nm and $l = 450$ nm is $\frac{J_{GB}}{J_s} > 40$. Hence, Eq. (1) thus reduces to:

$$\frac{\partial c_{i(v)}}{\partial t} = 0 = \xi_{FM} K_0 - \frac{4\pi r_{iv}}{\Omega} (D_i + D_v) c_{i(v)} c_{v(i)} - \frac{3\pi^2}{(d)^2} D_{i(v)} c_{i(v)}. \quad (2)$$

We next use Eq. (2) to obtain the concentration of vacancies and vacancy migration enthalpy; later we compare our results to the grain boundary model of IIC proposed by Ashkenazy and Averback [47].

The very weak temperature dependence of IIC observed in these HEA samples between ~ 100 °C and ~ 500 °C implies that in this temperature range the system resides in the so-called sink limited regime [49,50] and that the sink density and sink strength are constant. As the temperature is lowered, the point defect concentration increases and below 100 °C, the system falls into the recombination regime. In this regime, defect recombination limits the creep rate, giving rise to the temperature dependence of IIC. The transition from the recombination regime to the sink-limited regime thus occurs at ~ 100 °C, as illustrated in Fig. 7.

The activation energy for vacancy migration in the HEA can be determined by comparing the recombination term ($\frac{4\pi r_{iv}}{\Omega} (D_i + D_v) c_{i(v)} c_{v(i)}$) with the grain boundary sink elimination term ($\frac{3\pi^2}{(d)^2} D_{i(v)} c_{i(v)}$). At steady-state, $D_i c_i = D_v c_v$ [49], and so the ratio of these two terms can be expressed as:

$$f \approx 0.3 \approx \frac{4r_{iv} d^2}{3\pi \Omega} c_v \quad (3)$$

Solution to eq. 1(b) and Kinetic Monte Carlo (KMC) simulations have shown that at the transition temperature, T_t , from

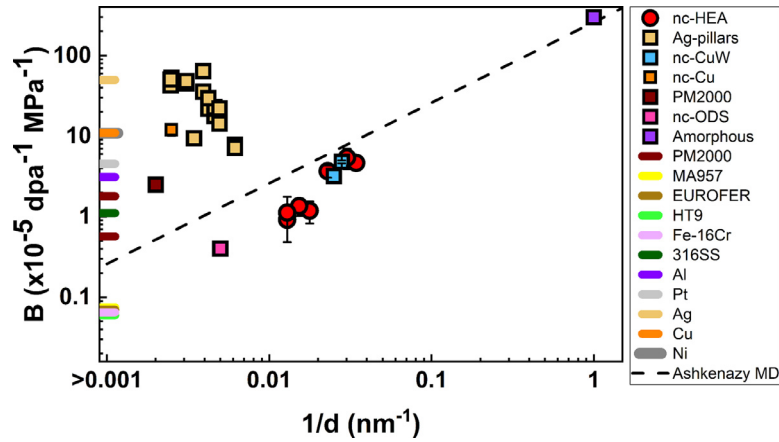


Fig. 8. IIC compliance (B) in the sink limited regime as a function of inverse grain size ($1/d$). The values from IIC of single crystalline Ag nanopillars [46], nanocrystalline CuW [58], and nano-ODS alloys [38], 19Cr-ODS [60], PM2000 [39], MA957 [61], HT9 [62], Fe-16Cr [63] and EUROFER [64] are also shown along with the compliance predicted from the MD simulation by Ashkenazy et al. [47].

the recombination limited regime to the sink-limited regime (see Fig. 7), $f \sim 0.30$ [51]. Since $d = 70$ nm and $r_{iv} \sim 2a_0$, [59] where $a_0 = 0.359$ nm [54] is the lattice parameter of NiCoFeCrMn, the irradiation-induced vacancy concentration at T_i is $c_v \sim 5.3 \times 10^{-7}$. The vacancy migration enthalpy can now be determined by substituting this value of c_v into the expression, $\xi_{FM}K_0 - \frac{3\pi^2}{d^2}D_v c_v = 0$, where $D_v = D_0 \exp(-\Delta H_m/kT)$, $D_0 = \frac{1}{6}a_0^2\nu$ and ν is the atomic jump attempt frequency (10^{14} s $^{-1}$). While ξ_{FM} is not known for NiCoFeCrMn, we will assume from the results of Naundorf et al. on Ni that it is ~ 0.01 [52,53]. Thus, using $K_0 = 1.9 \times 10^{-3}$ dpa/s, $T = 100$ °C, and $c_v = 5.3 \times 10^{-7}$, we obtain, $\Delta H_m = 0.71$ eV. We note, this calculation of ΔH_m is insensitive to ξ_{FM} ; for example, ΔH_m varies by only $\sim 10\%$ when ξ_{FM} changes by one order of magnitude. Choi et al. [54] calculated the migration enthalpy distribution of vacancies in NiCoFeCrMn using Canonical Monte-Carlo simulations. A distribution of migration energy barriers was obtained with a peak in the distribution between 0.67 eV and 0.87 eV, which thus agrees well with our experiments and analysis. The vacancy formation energy, ΔH_f , moreover, has been calculated for the 4 component NiCoFeCr alloy to be 1.7 eV [55]. Tracer diffusion measurements in NiCoFeCr yields activation energies, $Q = \Delta H_m + \Delta H_f$, varying between ≈ 2.5 eV for Co tracers and ≈ 3.3 eV for Cr tracers [56,57]. These experimental diffusion measurements in NiCoFeCr are thus also consistent with the value of ΔH_m deduced from our IIC measurements. At present, formation energies have not been determined in the 5 component system, where the activation energy for Co tracer diffusion, $Q \approx 2.8$ eV, is somewhat larger than in the 4 component system [56].

4.2. Comparison of IIC in nanocrystalline HEA to previously reported data in other systems

Fig. 8 compares the IIC compliance of the HEA films to other reported data from the literature with an emphasis on those obtained in the sink limit regime. With respect to grain size, the results on nanocrystalline Cu-1%W and Cu-6.5%W alloys reported in Ref. [58] most closely match the current study. Prior analysis of the Cu-W results suggests that the W precipitates in these alloys had no significant effect on the IIC compliance, other than to control the grain size, as the IIC compliances in the Cu-6.5%W and the Cu-1%W alloys were nearly the same despite the higher density of precipitates (4x) in the former [58]. The IIC compliances of the HEA and these Cu-W alloys are found to be the same, within experimental error, when normalized for grain size. Importantly, dislocation loops were not observed in either sample set. Therefore, it

is reasonable to assume that the same mechanism controls IIC in the two systems. Based on this hypothesis, we conclude that the defect production efficiencies of freely migrating Cu-W and HEA must be nearly the same. The IIC compliance of pure, large grain Cu samples [41], $d > 400$ nm, significantly exceeds the compliance measured in our nanocrystalline HEA and the nanocrystalline Cu-W. These samples, however, were observed to contain dislocation loops. Similarly, IIC compliance obtained from nano-ODS steels with larger grain size, $d \approx 250$ nm [38], lie somewhat above an extrapolated trend-line through our HEA data. These samples, however, were also found to contain dislocation loops [58,59], explaining the larger compliance. ODS steels with even larger grain sizes also have larger IIC compliances than our nanocrystalline HEA samples [39,60]. These results are interesting in view of prior work on IIC compliance of single crystalline Ag pillars. In these samples, the IIC compliance was size dependent. [46], i.e., the creep compliance was found to decrease with decreasing pillar size, and thus opposite the grain size effect observed here for nanocrystalline HEA. The size effect in the Ag pillars was attributed to the competition between dislocation sinks and surface sinks, the latter of which do not contribute to creep. From these overall data emerge general trends for the size dependence of IIC compliance in the sink limited regime. In the nanocrystalline regime, IIC compliance is controlled by a grain boundary mechanism, decreasing with increasing grain size, until the onset of loop nucleation at a critical grain size. Above this grain size, dislocation-based mechanisms begin to dominate and the IIC compliance increases with increasing grain size. Above a critical grain size, the fractional point defect flux to grain boundaries becomes negligible and all point defects annihilate at loops. This is shown schematically in supplementary Fig. S9.

4.3. IIC mechanism in nanocrystalline HEA

The model for IIC in nanocrystalline materials proposed by Ashkenazy and Averback [47] assumes that grain boundaries can be treated as an amorphous phase. Point defects absorbed in the grain boundary change the local atomic density, leading to relaxation to a more energetically favorable state, akin to shear transformation zones in amorphous metals. Since these relaxations are biased by the applied stress, they can eventually lead to creep under irradiation. Radiation-enhanced diffusion enters this model since point defects created in the grain interiors must migrate to the grain boundaries. At low temperatures, i.e., the recombination-limited regime, point defects mostly recombine and creep is suppressed. At high temperatures, i.e., above 100 °C in the present

experiments, all freely migrating defects reach the grain boundaries and creep becomes independent of temperature. An important prediction in this model is that the creep compliance varies as $1/d$, in contrast to Coble creep or Nabarro–Herring creep which vary as $1/d^3$ and $1/d^2$, respectively. As d becomes very small and approaches the grain boundary width in this model, the IIC compliance converges to the value for amorphous materials ($\sim 3 \text{ dpa}^{-1} \text{ GPa}^{-1}$). A comparison between this model and the experimental data is included in Fig. 8. The magnitude of the IIC compliance from the experiments correspond with the model predictions, especially considering no fitting parameters have been considered. It appears, however, that the slope of the experimental log (compliance)–log (grain size) curve, 1.8 ± 0.2 , is somewhat larger than the linear slope predicted by the model [47]. The model prediction of the absolute IIC compliance, moreover, is a factor of ~ 3 larger than that found experimentally; the model, however, assumes a mobile point defect production efficiency of $\xi_{FM} = 1$. It is now widely recognized the efficiency of total defect production in metals is $\sim 1/3$ [65–67], which if included in the model would result in excellent agreement with our experiments. We noted above, however, that measurements on large-grained metals indicate $\xi_{FM} \approx 0.01$. It has been suggested in nanocrystalline metals, however, that a high fraction of defects produced near grain boundaries are absorbed in the boundary [68–71], thus explaining the discrepancy. This possibility might also explain the super-linear slope observed in the experimental data in Fig. 8; i.e. a grain-size dependent production efficiency of freely migrating defects. The question of defect production efficiency, however, must remain for now an open question.

5. Conclusions

In summary, we have measured IIC during heavy ion irradiation in a nanocrystalline high entropy alloys for the first time using a calibrated high temperature *in situ* measurement technique. Our results indicate that IIC in nanocrystalline NiCoFeCrMn, with grain sizes $< 80 \text{ nm}$, enters the sink limited regime by 97°C during irradiation with 2.6 MeV Ag^{3+} at a dose rate of $1.5 \times 10^{-3} \text{ dpa}^{-1} \text{ s}^{-1}$. Thermal creep, in contrast, does not become comparable in magnitude until $\approx 650^\circ \text{C}$. In the sink limited regime, the grain size dependence suggests that a grain boundary mediated IIC mechanism is active, and the results are in reasonable agreement with a prior theoretical prediction. The magnitude of IIC compliance of the HEA is the same magnitude as previously reported for dilute nanocrystalline Cu alloys. The result suggests that the freely migrating point defect concentrations within the two nanocrystalline alloys are comparable at similar irradiation conditions indicating that recombination is not significantly enhanced in the nanocrystalline HEA.

Declaration of Competing Interest

The authors declare that they have no known competing financial interests or personal relationships that could have appeared to influence the work reported in this paper.

Acknowledgments

SJD, GSJ, and RSA were supported by the US DOE Office of Basic Energy Sciences, Materials Science and Engineering Division under Grant DE-SC0019875. CMB and KH were also supported by the DOE-BES Materials Science and Engineering Division, but under a separate FWP 15013170. This work was performed, in part, at the Center for Integrated Nanotechnologies, an Office of Science User Facility operated for the U.S. Department of Energy (DOE) Office

of Science. Sandia National Laboratories is a multimission laboratory managed and operated by National Technology & Engineering Solutions of Sandia, LLC, a wholly owned subsidiary of Honeywell International, Inc., for the U.S. DOE's National Nuclear Security Administration under contract DE-NA-0003525. The views expressed in the article do not necessarily represent the views of the U.S. DOE or the United States Government.

Supplementary material

Supplementary material associated with this article can be found, in the online version, at doi:10.1016/j.actamat.2019.10.022.

References

- [1] S.J. Zinkle, J.T. Busby, Structural materials for fission & fusion energy, Mater. Today 12 (2009) 12–19, doi:10.1016/S1369-7021(09)70294-9.
- [2] S.J. Zinkle, G.S. Was, Materials challenges in nuclear energy, Acta Mater. 61 (2013) 735–758, doi:10.1016/j.actamat.2012.11.004.
- [3] Y. Guerin, G.S. Was, S.J. Zinkle, Materials challenges for advanced nuclear energy systems, MRS Bull. 34 (2009) 10–14.
- [4] P. Ehrhart, R.S. Averback, Diffuse X-ray scattering studies of neutron- and electron-irradiated Ni, Cu and dilute alloys, Philos. Mag. A 60 (1989) 283–306, doi:10.1080/01418618908213863.
- [5] H. Wiedersich, Evolution of defect cluster distributions during irradiation, Mater. Sci. Forum 97–99 (1992) 59–74, doi:10.4028/www.scientific.net/MSF.97-99.59.
- [6] D.A. McClintock, M.A. Sokolov, D.T. Hoelzer, R.K. Nanstad, Mechanical properties of irradiated ODS-eurofer and nanocluster strengthened 14YWT, J. Nucl. Mater. 392 (2009) 353–359, doi:10.1016/j.jnucmat.2009.03.024.
- [7] E. Aydogan, N. Almirall, G.R. Odette, S.A. Maloy, O. Anderoglu, L. Shao, J.G. Gigax, L. Price, D. Chen, T. Chen, F.A. Garner, Y. Wu, P. Wells, J.J. Lewandowski, D.T. Hoelzer, Stability of nanosized oxides in ferrite under extremely high dose self ion irradiations, J. Nucl. Mater. 486 (2017) 86–95, doi:10.1016/j.jnucmat.2017.01.015.
- [8] J. Brodrick, D.J. Hepburn, G.J. Ackland, Mechanism for radiation damage resistance in yttrium oxide dispersion strengthened steels, J. Nucl. Mater. 445 (2014) 291–297, doi:10.1016/j.jnucmat.2013.10.045.
- [9] G.R. Odette, M.J. Alinger, B.D. Wirth, Recent developments in irradiation-resistant steels, Annu. Rev. Mater. Res. 38 (2008) 471–503, doi:10.1146/annurev.matsci.38.060407.130315.
- [10] S.J. Dillon, D.C. Bufford, G.S. Jawaharram, X. Liu, C. Lear, K. Hattar, R.S. Averback, Irradiation-induced creep in metallic nanolaminates characterized by *in situ* TEM pillar nanocompression, J. Nucl. Mater. 490 (2017) 59–65, doi:10.1016/j.jnucmat.2017.04.008.
- [11] S. Mao, S. Özerinç, W.P. King, R.S. Averback, S.J. Dillon, Effect of irradiation damage on the shear strength of Cu–Nb interfaces, Scr. Mater. 90 (2014) 29–32, doi:10.1016/j.scriptamat.2014.07.009.
- [12] M.J. Demkowicz, P. Bellon, B.D. Wirth, Atomic-scale design of radiation-tolerant nanocomposites, MRS Bull. 35 (2010) 992–998, doi:10.1557/mrs2010.704.
- [13] A. Misra, M. Verdier, Y.C. Lu, H. Kung, T.E. Mitchell, M. Nastasi, J.D. Embury, Structure and mechanical properties of Cu–x (X = Nb, Cr, Ni) nanolayered composites, Scr. Mater. 39 (1998) 555–560, doi:10.1016/S1359-6462(98)00196-1.
- [14] I.J. Beyerlein, A. Caro, M.J. Demkowicz, N.A. Mara, A. Misra, B.P. Uberuaga, Radiation damage tolerant nanomaterials, Mater. Today 16 (2013) 443–449, doi:10.1016/j.mattod.2013.10.019.
- [15] K. Hattar, M.J. Demkowicz, A. Misra, I.M. Robertson, R.G. Hoagland, Arrest of bubble growth in Cu–Nb multilayer nanocomposites, Scr. Mater. 58 (2008) 541–544, doi:10.1016/j.scriptamat.2007.11.007.
- [16] X. Zhang, N.Q. Vo, P. Bellon, R.S. Averback, Microstructural stability of nanostructured Cu–Nb–W alloys during high-temperature annealing and irradiation, Acta Mater. 59 (2011) 5332–5341, doi:10.1016/j.actamat.2011.05.009.
- [17] N.Q. Vo, S.W. Chee, D. Schwen, X. Zhang, P. Bellon, R.S. Averback, Microstructural stability of nanostructured Cu alloys during high-temperature irradiation, Scr. Mater. 63 (2010) 929–932, doi:10.1016/j.scriptamat.2010.07.009.
- [18] G.S. Jawaharram, S.J. Dillon, R.S. Averback, Hardening mechanisms in irradiated Cu–W alloys, J. Mater. Res. 32 (2017) 3156–3164, doi:10.1557/jmr.2017.295.
- [19] S.W. Chee, B. Stumph, N.Q. Vo, R.S. Averback, P. Bellon, Dynamic self-organization in Cu alloys under ion irradiation, Acta Mater. 58 (2010) 4088–4099, doi:10.1016/j.actamat.2010.03.039.
- [20] C. Lu, T. Yang, K. Jin, N. Gao, P. Xiu, Y. Zhang, F. Gao, H. Bei, W.J. Weber, K. Sun, Y. Dong, L. Wang, Radiation-induced segregation on defect clusters in single-phase concentrated solid-solution alloys, Acta Mater. 127 (2017) 98–107, doi:10.1016/j.actamat.2017.01.019.
- [21] C.M. Barr, J.E. Nathaniel, K.A. Unocic, J. Liu, Y. Zhang, Y. Wang, M.L. Taheri, Exploring radiation induced segregation mechanisms at grain boundaries in equiatomic CoCrFeNi high entropy alloy under heavy ion irradiation, Scr. Mater. 156 (2018) 80–84, doi:10.1016/j.scriptamat.2018.06.041.
- [22] P.R. Okamoto, L.E. Rehn, Radiation-induced segregation in binary and ternary alloys, J. Nucl. Mater. 83 (1979) 2–23, doi:10.1016/0022-3115(79)90587-7.
- [23] A.D. Marwick, R.C. Pillier, P.M. Sivel, Mechanisms of radiation-induced segregation in dilute nickel alloys, J. Nucl. Mater. 83 (1979) 35–41, doi:10.1016/0022-3115(79)90589-0.

- [24] R.A. Johnson, N.Q. Lam, Solute segregation in metals under irradiation, *Phys. Rev. B* 13 (1976) 4364–4375, doi:[10.1103/PhysRevB.13.4364](https://doi.org/10.1103/PhysRevB.13.4364).
- [25] T. Schuler, P. Bellon, D.R. Trinkle, R.S. Averback, Modeling the long-term evolution of dilute solid solutions in the presence of vacancy fluxes, *Phys. Rev. Mater.* 2 (2018) 073605, doi:[10.1103/PhysRevMaterials.2.073605](https://doi.org/10.1103/PhysRevMaterials.2.073605).
- [26] T. Schuler, D.R. Trinkle, P. Bellon, R. Averback, Design principles for radiation-resistant solid solutions, *Phys. Rev. B* 95 (2017), doi:[10.1103/PhysRevB.95.174102](https://doi.org/10.1103/PhysRevB.95.174102).
- [27] C. Lu, T. Yang, K. Jin, G. Velisa, P. Xiu, M. Song, Q. Peng, F. Gao, Y. Zhang, H. Bei, W.J. Weber, L. Wang, Enhanced void swelling in nicofercpd high-entropy alloy by indentation-induced dislocations, *Mater. Res. Lett.* 6 (2018) 584–591, doi:[10.1080/21663831.2018.1504136](https://doi.org/10.1080/21663831.2018.1504136).
- [28] S. Qin Xia, Z. Wang, T. fei Yang, Y. Zhang, Irradiation behavior in high entropy alloys, *J. Iron Steel Res. Int.* 22 (2015) 879–884, doi:[10.1016/S1006-706X\(15\)30084-4](https://doi.org/10.1016/S1006-706X(15)30084-4).
- [29] S.Q. Xia, X. Yang, T.F. Yang, S. Liu, Y. Zhang, Irradiation resistance in alNicoCrFeNi high entropy alloys, *Jom* 67 (2015) 2340–2344, doi:[10.1007/s11837-015-1568-4](https://doi.org/10.1007/s11837-015-1568-4).
- [30] C. Lu, L. Niu, N. Chen, K. Jin, T. Yang, P. Xiu, Y. Zhang, F. Gao, H. Bei, S. Shi, M.R. He, I.M. Robertson, W.J. Weber, L. Wang, Enhancing radiation tolerance by controlling defect mobility and migration pathways in multicomponent single-phase alloys, *Nat. Commun.* 7 (2016) 1–8, doi:[10.1038/ncomms13564](https://doi.org/10.1038/ncomms13564).
- [31] K. Jin, C. Lu, L.M. Wang, J. Qu, W.J. Weber, Y. Zhang, H. Bei, Effects of compositional complexity on the ion-irradiation induced swelling and hardening in Ni-containing equiatomic alloys, *Scr. Mater.* 119 (2016) 65–70, doi:[10.1016/j.scriptamat.2016.03.030](https://doi.org/10.1016/j.scriptamat.2016.03.030).
- [32] Tni Yang, C. Lu, G. Velisa, K. Jin, P. Xiu, Y. Zhang, H. Bei, L. Wang, Influence of irradiation temperature on void swelling in nicofercpd and nicofercpd, *Scr. Mater.* 158 (2019) 57–61, doi:[10.1016/j.scriptamat.2018.08.021](https://doi.org/10.1016/j.scriptamat.2018.08.021).
- [33] Y. Zhang, G.M. Stocks, K. Jin, C. Lu, H. Bei, B.C. Sales, L. Wang, L.K. B  land, R.E. Stoller, G.D. Samolyuk, M. Caro, A. Caro, W.J. Weber, Influence of chemical disorder on energy dissipation and defect evolution in concentrated solid solution alloys, *Nat. Commun.* 6 (2015), doi:[10.1038/ncomms9736](https://doi.org/10.1038/ncomms9736).
- [34] Y. Zhang, K. Jin, H. Xue, C. Lu, R.J. Olsen, L.K. B  land, M.W. Ullah, S. Zhao, H. Bei, D.S. Aidhy, G.D. Samolyuk, L. Wang, M. Caro, A. Caro, G.M. Stocks, B.C. Larson, I.M. Robertson, A.A. Correa, W.J. Weber, Influence of chemical disorder on energy dissipation and defect evolution in advanced alloys, *J. Mater. Res.* 31 (2016) 2363–2375, doi:[10.1557/jmr.2016.269](https://doi.org/10.1557/jmr.2016.269).
- [35] F. Granberg, K. Nordlund, M.W. Ullah, K. Jin, C. Lu, H. Bei, L.M. Wang, F. Djurabekova, W.J. Weber, Y. Zhang, Mechanism of radiation damage reduction in equiatomic multicomponent single phase alloys, *Phys. Rev. Lett.* 116 (2016) 1–8, doi:[10.1103/PhysRevLett.116.135504](https://doi.org/10.1103/PhysRevLett.116.135504).
- [36] B. Gludovatz, E.P. George, R.O. Ritchie, Processing, microstructure and mechanical properties of the crmfecon high-entropy alloy, *Jom* 67 (2015) 2262–2270, doi:[10.1007/s11837-015-1589-z](https://doi.org/10.1007/s11837-015-1589-z).
- [37] A.H.B. Gludovatz, D. Catoor, E.H. Chang, E.P. George, R.O. Ritchie, A fracture-resistant high-entropy alloy for cryogenic applications, *Science* 345 (2014) 1153–1158.
- [38] P. Jung, J. Chen, W. Hoffelner, A. Kimura, M.A. Pouchon, Irradiation creep and microstructural changes in an advanced ods ferritic steel during helium implantation under stress, *J. Nucl. Mater.* 386–388 (2008) 143–146, doi:[10.1016/j.jnucmat.2008.12.081](https://doi.org/10.1016/j.jnucmat.2008.12.081).
- [39] J. Chen, W. Hoffelner, Irradiation creep of oxide dispersion strengthened (ODS) steels for advanced nuclear applications, *J. Nucl. Mater.* 392 (2009) 360–363, doi:[10.1016/j.jnucmat.2009.03.025](https://doi.org/10.1016/j.jnucmat.2009.03.025).
- [40] S.   zerin  , R.S. Averback, W.P. King, In situ measurements of irradiation-induced creep of nanocrystalline copper at elevated temperatures, *Jom* 68 (2016) 2737–2741, doi:[10.1007/s11837-016-2077-9](https://doi.org/10.1007/s11837-016-2077-9).
- [41] K. Tai, R.S. Averback, P. Bellon, Y. Ashkenazy, Irradiation-induced creep in nanostructured Cu alloys, *Scr. Mater.* 65 (2011) 163–166, doi:[10.1016/j.scriptamat.2011.04.001](https://doi.org/10.1016/j.scriptamat.2011.04.001).
- [42] S.   zerin  , H.J. Kim, R.S. Averback, W.P. King, Direct measurements of irradiation-induced creep in micropillars of amorphous Cu₅₆Ti₃₈Ag₆, Zr₅₂Ni₄₈, Si, and SiO₂, *J. Appl. Phys.* 117 (2015), doi:[10.1063/1.4905019](https://doi.org/10.1063/1.4905019).
- [43] P. Hosemann, C. Shin, D. Kiener, I. Introduction, Small scale mechanical testing of irradiated materials, 30 (2017) 1231–1245, doi:[10.1557/jmr.2015.26](https://doi.org/10.1557/jmr.2015.26).
- [44] P. Lapouge, F. Onimus, R. Vayrette, T. Pardo, A novel on chip test method to characterize the creep behavior of metallic layers under heavy ion irradiation, *J. Nucl. Mater.* 476 (2016) 20–29, doi:[10.1016/j.jnucmat.2016.04.014](https://doi.org/10.1016/j.jnucmat.2016.04.014).
- [45] M. Gaum  , P. Baldo, F. Momp  u, F. Onimus, In-situ observation of an irradiation creep deformation mechanism in zirconium alloys, *Scr. Mater.* 154 (2018) 87–91, doi:[10.1016/j.scriptamat.2018.05.030](https://doi.org/10.1016/j.scriptamat.2018.05.030).
- [46] G.S. Jawaharrram, P.M. Price, C.M. Barr, K. Hattar, R.S. Averback, S.J. Dillon, High temperature irradiation induced creep in Ag nanopillars measured via *in situ* transmission electron microscopy, *Scr. Mater.* 148 (2018) 1–4, doi:[10.1016/j.scriptamat.2018.01.007](https://doi.org/10.1016/j.scriptamat.2018.01.007).
- [47] Y. Ashkenazy, R.S. Averback, Irradiation induced grain boundary flow – A new creep mechanism at the nanoscale, *Nano Lett.* 12 (2012) 4084–4089, doi:[10.1021/nl301554k](https://doi.org/10.1021/nl301554k).
- [48] K. Hattar, D.C. Bufford, D.L. Buller, Concurrent *in situ* ion irradiation transmission electron microscope, *Nucl. Instrum. Methods Phys. Res. Sect. B Beam Interact. Mater. Atoms* 338 (2014) 56–65, doi:[10.1016/j.nimb.2014.08.002](https://doi.org/10.1016/j.nimb.2014.08.002).
- [49] R. Sizmann, The effect of radiation upon diffusion in metals, *J. Nucl. Mater.* 69–70 (1978) 386–412, doi:[10.1016/0022-3115\(78\)90256-8](https://doi.org/10.1016/0022-3115(78)90256-8).
- [50] S. Mao, S. Shu, J. Zhou, R.S. Averback, S.J. Dillon, Quantitative comparison of sink efficiency of Cu–Nb, Cu–V and Cu–Ni interfaces for point defects, *Acta Mater.* 82 (2015) 328–335, doi:[10.1016/j.actamat.2014.09.011](https://doi.org/10.1016/j.actamat.2014.09.011).
- [51] S. Shu, P. Bellon, R.S. Averback, Role of point-defect sinks on irradiation-induced compositional patterning in model binary alloys, *Phys. Rev. B – Condens. Matter Mater. Phys.* 91 (2015) 1–13, doi:[10.1103/PhysRevB.91.214107](https://doi.org/10.1103/PhysRevB.91.214107).
- [52] V. Naundorf, M.-P. Macht, H. Wollenberger, Production rate of freely migrating defects for ion irradiation, *J. Nucl. Mater.* 186 (1992) 227–236, doi:[10.1016/0022-3115\(92\)90340-Q](https://doi.org/10.1016/0022-3115(92)90340-Q).
- [53] L.E. Rehn, P.R. Okamoto, R.S. Averback, Relative efficiencies of different ions for producing freely migrating defects, *Phys. Rev. B* 30 (1984) 3073–3080, doi:[10.1103/PhysRevB.30.3073](https://doi.org/10.1103/PhysRevB.30.3073).
- [54] W.M. Choi, Y.H. Jo, S.S. Sohn, S. Lee, B.J. Lee, Understanding the physical metallurgy of the cocrfemni high-entropy alloy: an atomistic simulation study, *Npj Comput. Mater.* 4 (2018) 1–9, doi:[10.1038/s41524-017-0060-9](https://doi.org/10.1038/s41524-017-0060-9).
- [55] W. Chen, X. Ding, Y. Feng, X. Liu, K. Liu, Z.P. Lu, D. Li, Y. Li, C.T. Liu, X.Q. Chen, Vacancy formation enthalpies of high-entropy fecocrni alloy via first-principles calculations and possible implications to its superior radiation tolerance, *J. Mater. Sci. Technol.* 34 (2018) 355–364, doi:[10.1016/j.jmst.2017.11.005](https://doi.org/10.1016/j.jmst.2017.11.005).
- [56] D. Gaertner, J. Kottke, G. Wilde, S.V. Divinski, Y. Chumlyakov, Tracer diffusion in single crystalline cocrfeni and cocrfemni high entropy alloys, *J. Mater. Res.* 33 (2018) 3184–3191, doi:[10.1557/jmr.2018.162](https://doi.org/10.1557/jmr.2018.162).
- [57] M. Vaidya, G. Mohan Muralikrishna, S.V. Divinski, B.S. Murty, Experimental assessment of the thermodynamic factor for diffusion in cocrfeni and cocrfemni high entropy alloys, *Scr. Mater.* 157 (2018) 81–85, doi:[10.1016/j.scriptamat.2018.07.040](https://doi.org/10.1016/j.scriptamat.2018.07.040).
- [58] K. Tai, R.S. Averback, P. Bellon, Y. Ashkenazy, B. Stumphy, Temperature dependence of irradiation-induced creep in dilute nanostructured Cu–W alloys, *J. Nucl. Mater.* 422 (2012) 8–13, doi:[10.1016/j.jnucmat.2011.11.068](https://doi.org/10.1016/j.jnucmat.2011.11.068).
- [59] J. Chen, P. Jung, W. Hoffelner, H. Ullmaier, Dislocation loops and bubbles in oxide dispersion strengthened ferritic steel after helium implantation under stress, *Acta Mater.* 56 (2008) 250–258, doi:[10.1016/j.actamat.2007.09.016](https://doi.org/10.1016/j.actamat.2007.09.016).
- [60] J. Chen, P. Jung, W. Hoffelner, Irradiation creep of candidate materials for advanced nuclear plants, *J. Nucl. Mater.* 441 (2013) 688–694, doi:[10.1016/j.jnucmat.2013.04.024](https://doi.org/10.1016/j.jnucmat.2013.04.024).
- [61] M.B. Toloczko, F.A. Garner, S.A. Maloy, Irradiation creep and density changes observed in MA957 pressurized tubes irradiated to doses of 40–110 dpa at 400–750   C in ftf, *J. Nucl. Mater.* 428 (2012) 170–175, doi:[10.1016/j.jnucmat.2012.04.005](https://doi.org/10.1016/j.jnucmat.2012.04.005).
- [62] M.B. Toloczko, D.S. Gelles, F.A. Garner, R.J. Kurtz, K. Abe, Irradiation creep and swelling from 400 to 600   C of the oxide dispersion strengthened ferritic alloy MA957, *J. Nucl. Mater.* 329–333 (2004) 352–355, doi:[10.1016/j.jnucmat.2004.04.296](https://doi.org/10.1016/j.jnucmat.2004.04.296).
- [63] M.L. Grossbeck, L.T. Gibson, S. Jitsukawa, Irradiation creep in austenitic and ferritic steels irradiated in a tailored neutron spectrum to induce fusion reactor levels of helium, *J. Nucl. Mater.* 233–237 (1996) 148–151, doi:[10.1016/S0022-3115\(96\)00205-X](https://doi.org/10.1016/S0022-3115(96)00205-X).
- [64] A. Alamo, J.L. Bertin, V.K. Shamardin, P. Wident, Mechanical properties of 9Cr martensitic steels and ODS–FeCr alloys after neutron irradiation at 325  C up to 42dpa, *J. Nucl. Mater.* 367–370 (2007) 54–59, doi:[10.1016/j.jnucmat.2007.03.166](https://doi.org/10.1016/j.jnucmat.2007.03.166).
- [65] R.S. Averback, R. Benedek, K.L. Merkle, Ion-irradiation studies of the damage function of copper and silver, *Phys. Rev. B* 18 (1978) 4156–4171, doi:[10.1103/PhysRevB.18.4156](https://doi.org/10.1103/PhysRevB.18.4156).
- [66] R.S. Averback, T.D. de la Rubia, Displacement damage in irradiated metals and semiconductors, *Solid State Phys. – Adv. Res. Appl.* 51 (1997) 281–402, doi:[10.1016/S0081-1947\(08\)60193-9](https://doi.org/10.1016/S0081-1947(08)60193-9).
- [67] K. Nordlund, S.J. Zinkle, A.E. Sand, F. Granberg, R.S. Averback, R. Stoller, T. Suzudo, L. Malerba, F. Banhart, W.J. Weber, F. Willaime, S.L. Dudarev, D. Simeone, Improving atomic displacement and replacement calculations with physically realistic damage models, *Nat. Commun.* 9 (2018) 1084, doi:[10.1038/s41467-018-03415-5](https://doi.org/10.1038/s41467-018-03415-5).
- [68] X.-M. Bai, A.F. Voter, R.G. Hoagland, M. Nastasi, B.P. Uberuaga, Efficient annealing of radiation damage near grain boundaries via interstitial emission, *Science* (80-) 327 (2010) 1631–1634, doi:[10.1126/science.1183723](https://doi.org/10.1126/science.1183723).
- [69] X.-M. Bai, L.J. Vernon, R.G. Hoagland, A.F. Voter, M. Nastasi, B.P. Uberuaga, Role of atomic structure on grain boundary-defect interactions in Cu, *Phys. Rev. B* 85 (2012) 214103, doi:[10.1103/PhysRevB.85.214103](https://doi.org/10.1103/PhysRevB.85.214103).
- [70] F. Gao, D. Chen, W. Hu, W.J. Weber, Energy dissipation and defect generation in nanocrystalline silicon carbide, *Phys. Rev. B* 81 (2010) 184101, doi:[10.1103/PhysRevB.81.184101](https://doi.org/10.1103/PhysRevB.81.184101).
- [71] M.J. Demkowicz, O. Anderoglu, X. Zhang, A. Misra, The influence of Σ 3 twin boundaries on the formation of radiation-induced defect clusters in nanotwinned Cu, *J. Mater. Res.* 26 (2011) 1666–1675, doi:[10.1557/jmr.2011.56](https://doi.org/10.1557/jmr.2011.56).